Favorable Impact Toughness of High Heat Input Coarse-Grained HAZ in an Ultra-Low Carbon High-Strength Microalloyed Steel

Yulong Yang[1] · Xiao Jia[2] · Yaxin Ma[2] · Ping Wang[1] · Fuxian Zhu[2]

Abstract

An ultra-low carbon (0.035 wt%) high-strength steel plate was produced. The coarse-grained heat-affected Zone (CGHAZ) was simulated with different heat inputs of 25–200 kJ/cm. The low-temperature impact toughness and microstructure of CGHAZ were analyzed. The results indicated that the impact toughness of CGHAZ exhibited a favorable value at −20 °C under high heat input conditions. The Ti-containing complex inclusions stimulated the crack initiation and induced the nucleation of acicular microstructure. With the increase of heat inputs, the morphology of carbides or martensite–austenite (M–A) constituents changed from strip to block gradually, and the volume fraction decreased gradually, which increased the crack initiation absorbed energy. The coarse grain boundary ferrite (GBF) occupied by massive low-angle grain boundaries was not conducive to the crack propagation absorbed energy. In addition, the kinetic effective activation energy of GBF and acicular ferrite/granular bainite (AF/GB) were calculated to be ~175 kJ/mol and ~227 kJ/mol respectively, which revealed the kinetic reason for the preferential precipitation of GBF.

Keywords High heat input · CGHAZ · M–A constituents · Toughness · Inclusion

1 Introduction

In recent years, with the increase of high efficiency welding requirement for high-strength plates in the industrial fields, low carbon microalloyed steel with superior strength and toughness obtained by thermomechanical controlling processing (TMCP) technology has become the preferred base material of choice. The welding performance of high-strength base metal (BM) has been attach much attention in related fields [1–3]. Although reasonable metallurgical methods and thermal processing technology are used to improve the comprehensive mechanical properties of BM to promote welding adaptability [4–7], The deterioration of low-temperature impact toughness of the welded joints has always been a worrying issue [8–10].

As is known, Welding heat-affected zone (HAZ) is the inescapable position of the welded joint, which is composed of intercritical HAZ (ICHAZ), fine-grained HAZ (FGHAZ) and coarse-grained CGHAZ [11–13]. The CGHAZ is the most affected by the higher peak temperature (generally 1350–1400 °C), and the mechanical properties of CGHAZ have the greatest tendency to deteriorate. Therefore, the CGHAZ has become the most important position of concern [14, 15]. Numerous references have focused on the micro-mechanism and influencing factors of CGHAZ toughness deterioration in order to improve the low-temperature impact toughness as much as possible [1, 9, 16].

As far as the welding process is concerned, the heat input is a very critical technical parameter, which has an important influence on the microstructure and impact toughness of CGHAZ [9, 12]. It characterizes the heat energy absorbed by the welding process per unit length. The heat input is related to the current, voltage and welding speed [8, 17]. Although high heat input welding can improve the production efficiency, it also causes the longer high-temperature austenitization residence and slower cooling rate, which has an important influence on the microstructure and element diffusion behavior of CGHAZ [9, 18–20]. Relevant studies have shown that the toughness of CGHAZ is related to the

✉ Ping Wang
wang20211107@126.com

1 Key Laboratory of Electromagnetic Processing of Materials, Ministry of Education, Northeastern University, Shenyang 110819, China

2 State Key Laboratory of Rolling and Automation, Northeastern University, Shenyang 110819, China

M–A constituents, GBF and AF et al. [21–23]. Ramachandran et al. studied the comprehensive effects of M–A constituents and boundary microstructure on the toughness of CGHAZ in low carbon high-strength steel plates under high heat input conditions and pointed out that the segregation of carbon atoms at the grain boundaries results in a large number of blocky M–A constituents due to the influence of high heat input. Besides, the M–A constituents, which together with the coarse GBF and GB reduce the toughness of CGHAZ [22]. Zhou et al. also pointed out that although the high-angle grain boundaries can hinder the crack propagation effectively, the massive M–A constituents precipitated at the grain boundaries always reduce the absorbed energy of crack initiation [24]. It can be seen that it is not easy to obtain favorable CGHAZ toughness under high heat input welding conditions. Therefore, the research on the improvement of CGHAZ toughness is particularly important.

For high-strength BM, the deterioration of CGHAZ toughness is more serious under high heat input conditions, because the increasing strength of BM is at the expense of the increase of carbon equivalent, which will inevitably lead to a large amount of brittle-hardening phases such as carbides or M–A islands. This is not conducive to the improvement of CGHAZ toughness [23, 25]. Mohseni et al. pointed out that for high-strength steel with a carbon content of 0.06 wt%, the hardness value of the M–A constituent is between 600 HV and 1000 HV, which is significantly higher than the surrounding matrix, and the carbon concentration of the M–A constituents is also higher than that of the matrix [1, 22]. Under the condition of high heat input welding, although the reasonable microalloying will promote the formation of a certain amount of AF microstructure in the prior austenite grains due to the effect of heterogeneous nucleation, it also provides greater driving force for the nucleation of massive GBF microstructure. The coarse blocky BF is not conducive to the improvement of impact toughness [26]. Based on the ultra-high heat input of 800 kJ/cm in a low-carbon high-strength steel, Shi et al. pointed out that the austenite grain size of CGHAZ increases significantly, while the proportion of AF microstructure is greatly reduced. Besides, a large amount of GBF precipitates at the grain boundary, which significantly reduces the toughness of CGHAZ [27]. Lan et al. studied the CGHAZ toughness of a 690 MPa high-strength bainite steel and believed that the main reason for the decrease of toughness, on the one hand, is the change of the size and shape of M–A constituents, which provides convenience for the crack initiation; On the other hand, the high-angle boundary within the coarse austenite grains is reduced, which decreases the hindrance of crack propagation [28]. Therefore, the effective control of the ratio of acicular microstructure and boundary microstructure in CGHAZ is the key factor for obtaining excellent toughness of CGHAZ under high heat input conditions.

According to the Chinese national standard GB/T712-2011, a favorable impact toughness value of CGHAZ at any heat inputs should be greater than 46 J at −20 °C, which corresponds to the D-grade ocean engineering structural steels. For 690 MPa high-strength steel, most of the researches are mainly focused on the mechanism of toughness deterioration and influencing factors. It is not easy to obtain favorable CGHAZ toughness under high heat input conditions. In this paper, based on the "oxide metallurgy" and TMCP technology, the carbon content and carbon equivalent were controlled reasonably and the Nb element was prevented strictly to avoid more carbide enrichment under high heat input conditions. Only reasonable two-stage rolling process (TMCP technology) was used to ensure the comprehensive mechanical properties of the base metals. In addition, the ideal oxide inclusions were obtained by Ti/Al/V deoxidation/nitrogen controlling methods, which gave full play to the role of inducing AF nucleation under high heat input conditions. The main purpose is to effectively control the acicular microstructure and boundary microstructure in CGHAZ. Successfully, an ultra-low carbon (0.035 wt%) high-strength steel plates with the yield strength of ~690 MPa was produced in the laboratory. The analysis of the microstructure and impact toughness of simulated CGHAZ with different high heat inputs were carried out, which provided a new theoretical idea and industrial guiding significance for the research of low carbon high strength steel used for high heat input welding conditions.

2 Materials and Methods

The investigated steel was obtained through an electromagnetic induction heating furnace in the laboratory based on "oxide metallurgy" technology. The main precautions and process are as follows: The category, content and addition order of alloying elements were strictly controlled during the melting process. Cr, Ni, Cu were selected as the main strengthening elements, and the addition of Nb was prohibited; The carbon content in the molten steel during the melting process was strictly controlled to ensure low-carbon design principles; The whole deoxidation/nitrogen of melting process was carried out strictly in the order of Si, Mn, Al and Ti/V to ensure the oxygen content at each stage to obtain ideal oxide inclusions in the molten steel. The weight of the solidified ingot was ~20Kg. After removing the defects of heads and tails, the ingots were homogenized by heating to austenite temperature zone, and then forged into the square blank of 80 × 80 mm respectively. The main chemical composition of the investigated steel is shown in Table 1.

After holding for 6 h at 1250 °C, the blank was rolled through a Ø450 × 450 Two-high Reversing Hot Rolling Mill based on the TMCP technology. The rolling temperature in

Table 1 Main chemical composition of the investigated steels (wt%)

C	Si	Mn	Al	≤P	≤S	Ti/V	Cr/Ni/Cu
0.035	0.2	1.7	0.013	0.009	0.007	0.04	1.45

Table 2 Average values of basic mechanical properties of the investigated steel

Yield strength/ MPa	Tensile strength/MPa	Uniform elongation/%	Impact energy/J (−20 °C)
~ 678	~ 764	~ 11.9	~ 192

austenite recrystallization and non-recrystallized zone were controlled above 1150 °C and 800–850 °C respectively. The final rolled plate was cooled to room temperature by water and tempered at 350 °C for 1 h. The final plate thickness was ~13 mm, and the tensile/impact tests were conducted according to the international standard ISO 6892-1 and ISO 148-1. The average values of basic mechanical properties are shown in Table 2.

All sampling processes were as close to the center of the plate as possible, and the welding thermal simulation were sampled parallel to the rolling direction with the size of $11 \times 11 \times 55$ mm. Gleeble 3800 thermal simulator was used to simulate the CGHAZ with different heat inputs. Rykalin-2D curve model was used in the welding thermal simulation, under which the cooling time from 800 °C to 500 °C ($t_{8/5}$) during the welding thermal cycle was obtained by different heat inputs and relevant parameters. The curves and parameters of welding thermal simulation are shown in Fig. 1 (air cooling below 400 °C was used to save experimental time).

The samples subjected to the welding thermal simulation were machined to the size of 10 mm $\times$ 10 mm $\times$ 55 mm. Charpy impact test was carried out on an instrumented impact testing machine at −20 °C according to the international standard ISO 148-1. Dilatometric test was conducted using a Formastor-FⅡ machine to analyse the phase transformation dynamics of CGHAZ under different heat inputs. The size of the sample was φ3 $\times$ 10 mm and the equivalent welding thermal cycles of different heat inputs are shown in Fig. 2 (air cooling below 400 °C was used to save experimental time).

The metallographic specimens of simulated CGHAZ were ground and polished. The microstructure and chemical composition were analyzed by Optical Microscope (OM) and Electron Probe Micro-analyzer (EPMA) after being etched by 4% nital. A Field Emission Scanning Electron Microscope (FE-SEM ZEISS Ultra-55) equipped with EBSD technology was used to analyze the crystallographic orientation. The step size was set to 1 μm. The scanning magnification was 200 times. The EBSD samples were
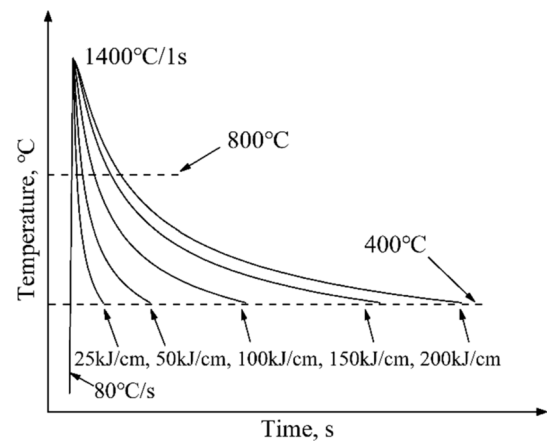
Fig. 1 Cooling curves of welding thermal simulation with different heat inputs
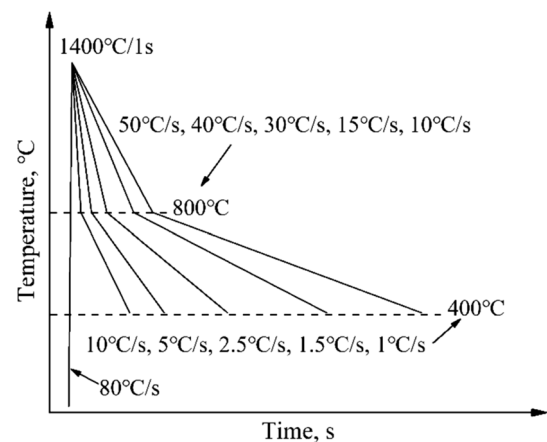
Fig. 2 Equivalent welding thermal cycling process of different heat inputs based on dilatometric test

electropolished with 12.5% perchloric acid ethanol solution to remove the surface stress layer. The HKL Channel 5 software was adopted for data processing. A Field Emission Transmission Electron Microscope (FETEM) was used to observe the substructure with the output voltage of 200 keV. The thin film sample used for TEM detection was manually polished to within the thickness of 0.05 mm and then punched into a φ3 disc. Twin-jet electropolisher equipment was used for further double-jet thinning process. The electrolyte was 90% acetic acid and 10% perchloric acid.

3 Results and Discussion

3.1 Microstructure and Phase Transformation

Figure 3 shows the microstructure of CGHAZ at different heat inputs. As can be seen from Fig. 3a, there is no obvious AF observed at 25 kJ/cm condition, the microstructure is mainly occupied by GB and a large amount of carbides. With the increase of heat input, the intragranular acicular microstructure appears gradually and the AF and GB can not be clearly distinguished in the prior austenite grains. However, the size of GB packets seems to change apparently with the increase of heat input. At 25 kJ/cm, no obvious GB packets are observed because the GBF is almost absent. With the increase of heat input, the GB packets gradually appear and show the maximum size at 100 kJ/cm. However, when the heat input continues to increase to 200 kJ/cm, the GB packets are segmented by a large number of GBF and the size decreases to some extent. In addition, compared with lower heat input conditions, the carbide enrichment under high heat input is affected by the formation of GBF and mainly concentrates in the interior of GB packets, which is obviously affected by the diffusion of carbon atoms under high heat input conditions. It's also worth noting that the average size of prior austenite grain was only ~60 μm at 25 kJ/cm. With the increase of heat input, the prior austenite grains were coarsened significantly. When the heat input reached 200 kJ/cm, massive GBF was precipitated, making it different to distinguish the prior austenite grains (Fig. 3e). Most of the observed prior austenite grains was close to ~200 μm approximately as shown the blue dotted grain in Fig. 3e

The effect of heat input on microstructure is mainly manifested in the formation of AF, the size of GB packets and the precipitation of carbides. It is generally believed that AF is a special bainite with a slightly higher phase transformation temperature affected by heterogeneous nucleation and shear mechanism, which is related to the cooling rate [10, 29, 30]. At the low heat input of 25 kJ/cm, the cooling rate is relatively fast. The AF has no time to meet the heteronucleation condition at the higher temperature and quickly enters the bainite phase transformation zone. Liu et al. also believed that bainite transformation occurs faster at lower heat input, and the bainite transformation includes two processes of bainite ferrite and the precipitation of carbides [31]. At fast cooling rate, the diffusion of carbon atoms is relatively slower, resulting in the dispersed carbide precipitation to be formed easily. This lead to the bainite laths to be divided by a large number of carbide to form GB microstructure as shown in Fig. 3a. Therefore, for the low carbon and high strength microalloyed steel, low heat input is favorable to

the formation of GB, but unfavorable to the precipitation of AF. This is consistent with the microstructure obtained by Lan et al. at lower heat inputs [28].

However, under the condition of high heat inputs, the driving force for atomic diffusion increases due to the prolonged residence time at high temperature, which not only intensifies the probability of migration of the PAGB to cause the coarser austenite grains, but also stimulates a large amount of GBF precipitates at the boundaries [27]. Slower cooling rate, on the one hand, is favorable for AF nucleation under the combined influence of heterogeneous nucleation and shear-diffusion mechanisms [5], on the other hand, the carbon atoms are able to migrate sufficiently from the interface to the interior of the grains to form the denser carbide enrichment. Massive GBF microstructure occupies most of the growth space of intracranular needle-like microstructures under high heat input conditions, and the two inhibit each other to form the complex GB packets, as shown in Figs. 3b–e. Therefore, the size of GB packet is affected by the prior austenite grains and GBF content. The results are also basically in line with the researches of Zhang and Shin et al. [3, 26].

The static dilatometric test was used to capture the slight change of volume of thermal expansion during the phase transformation, and the dynamic curves were obtained during the cooling process at different heat inputs. As shown in Fig. 4a, the approximate straight sections at both ends of the curves represent that the phase transformation have not yet occurred and have been completed respectively during the cooling process. It can be seen that the phase transformation process is mainly concentrated at 460–680 °C, which shows a typical bainite-ferrite transformation regions. The starting and finishing temperatures of the phase transformation under different heat inputs are shown in the figure embedded in Fig. 4a. As the heat input increases, the starting temperature increases gradually, while the finishing temperature do not change significantly. It can be seen that the heat input has a greater influence on the starting temperature than finishing temperature, which is directly related to the precipitation of GBF as shown in Fig. 3.

According to the classical lever principle of thermal expansion curve, the volume fraction transformed with temperature f_v^T at a given temperature can be obtained by formula (1) [15, 32].

$$f_v^T = \frac{\Delta L/L_0(T) - \Delta L_b/L_0(T)}{\Delta L_a/L_0(T) - \Delta L_b/L_0(T)} \tag{1}$$

The corresponding physical meanings of the mathematical symbols in formula (1) are shown in Fig. 4a, where $\Delta L/L_0(T)$ is the total linear thermal expansion rate after the phase transformation occurred completely at temperature T. $\Delta L_b/L_0(T)$ and $\Delta L_a/L_0(T)$ represent the corresponding values
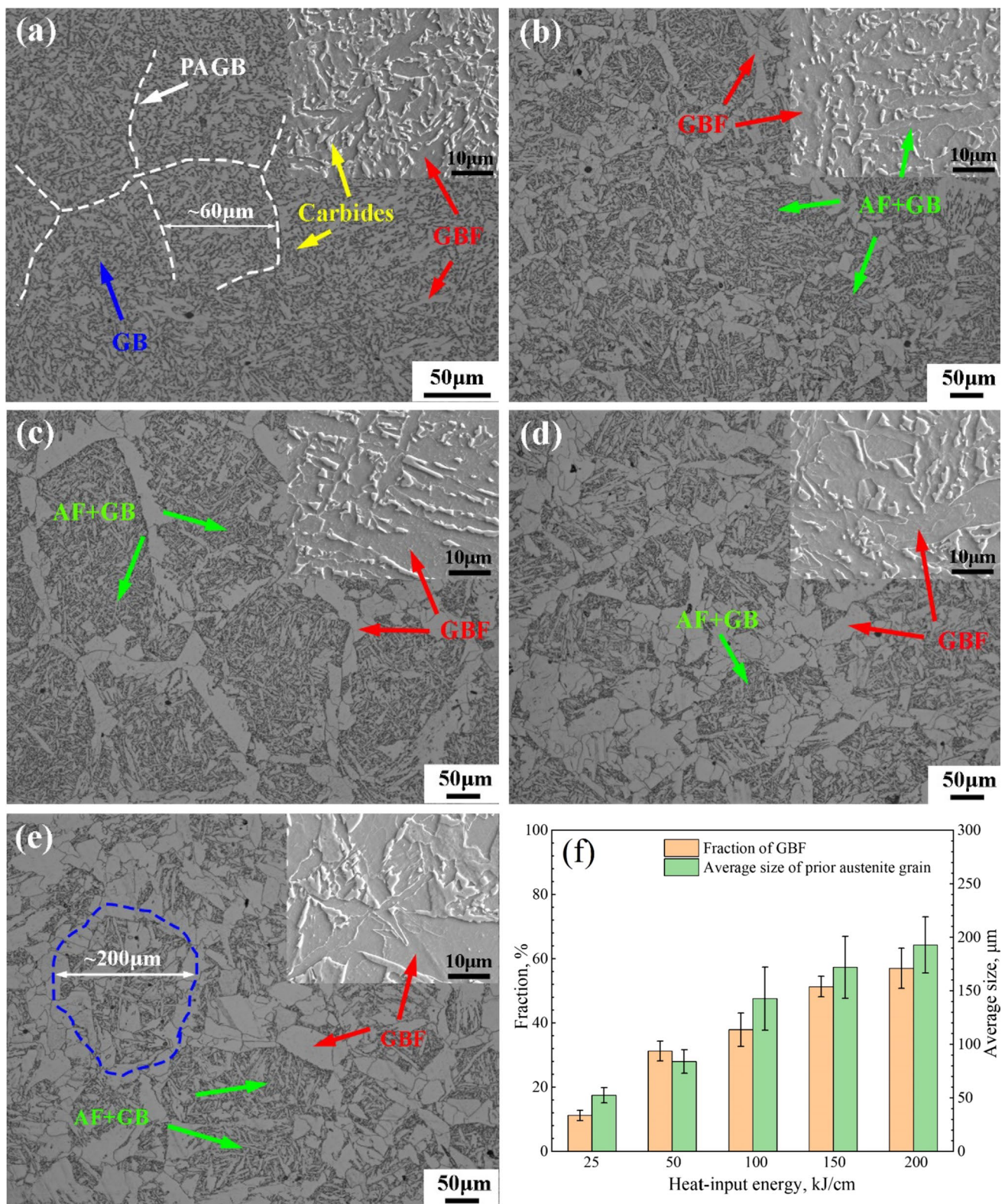
Fig. 3 Microstructure and statistical data under different heat input conditions. **a** 25 kJ/cm; **b** 50 kJ/cm; **c** 100 kJ/cm; **d** 150 kJ/cm; **e** 200 kJ/cm; **f** Statistical data. The embedded images show the electronic microstructure at larger magnification. PAGB: Prior austenite grain boundary
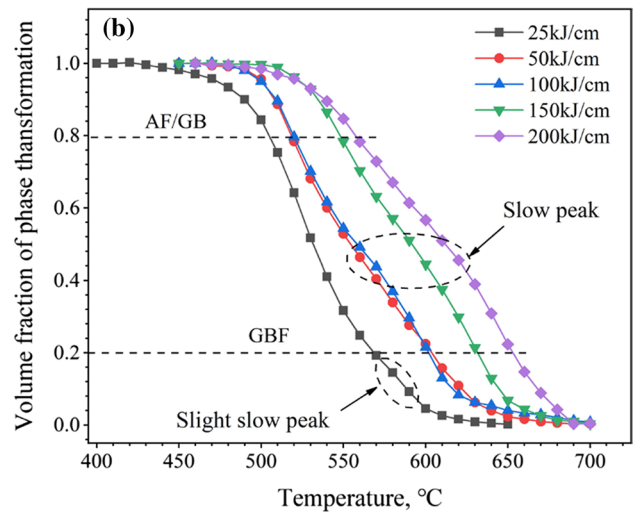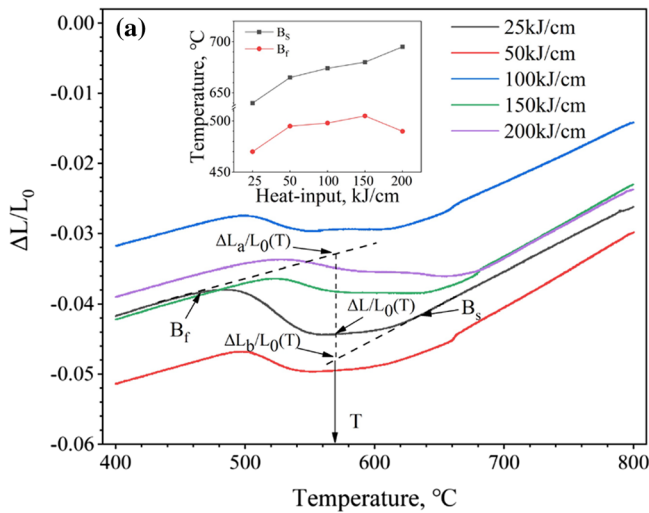
Fig. 4 Phase transformation of BM at different heat inputs during cooling process based on dilatometric test. **a** Typical dilatometric curves; **b** Volume fraction of the phase transformation varies with temperature; The figure embedded in Fig. 4a shows the change of initial (B_s) and final temperatures (B_f) of phase transformation

at the beginning and finishing moments of phase transformation respectively. According to the calculation results shown in Fig. 4b, Rapid phase transformation rate is observed at heat input of 25 kJ/cm, which seems mainly to be affected by the complete GB microstructure under this conditions. However, as the heat input increases, the formation of GBF and AF/GB packets cause the rate of phase transformation to slow down. This is related to the fact that GBF occupies most of the AF/GB growth areas in the prior austenite grain [3]. It is worth noting that different degrees of slow peaks was observed on all the curves in Fig. 4b, which indicates the formation of new phases. Considering that the effective activation energy of phase transformation is a constant that will not be changed with the transformed volume fraction and cooling rate, the effective activation energy of different phases can be estimated through the linear regression curve of $Ln\frac{T_f^2}{\Phi}$ vs. $\frac{1}{T_f}$ in formula (2) [15, 29, 30, 33].

$$Ln\frac{T_f^2}{\Phi} = \frac{E_a}{R} \cdot \frac{1}{T_f} + C \qquad (2)$$

where T_f is the temperature corresponding to a fixed percent of transformation completion; Φ is the cooling rate under different heat inputs corresponding to $t_{8/5}$ in Fig. 2. Ea is the effective activation energy, R is the gas constant and C is the constant. Combining the microstructure and phase transformation rate in Figs. 3 and 4b, the effective activation energies of GBF and AF/GB were calculated with the transformed volume fractions of 20% and 80%. The results are shown in Fig. 5. It can be seen that the effective activation energy of GBF is ~175 kJ/mol, while the value of AF/GB is slightly higher of ~227 kJ/mol. This explains the reason for
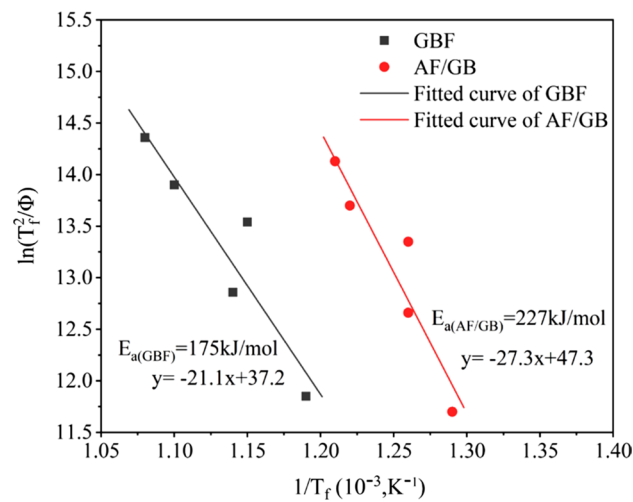

Fig. 5 Fitted curves of effective activation energy of phase transformation. E_a: Effective activation energy

the preferential precipitation of GBF under high heat input conditions from the perspective of kinetics, and it is also the key to influence the mechanical properties of CGHAZ. The calculation results are similar to the research of Gupta et al. on the kinetics of phase transformation during continuous cooling of bainite [29].

3.2 Impact Toughness

Figure 6 shows the impact performance of the samples at −20 °C under different heat inputs. As can be seen, the average value of impact energy is ~158 J at 25 kJ/cm. With the increase of the heat input, the average values decrease
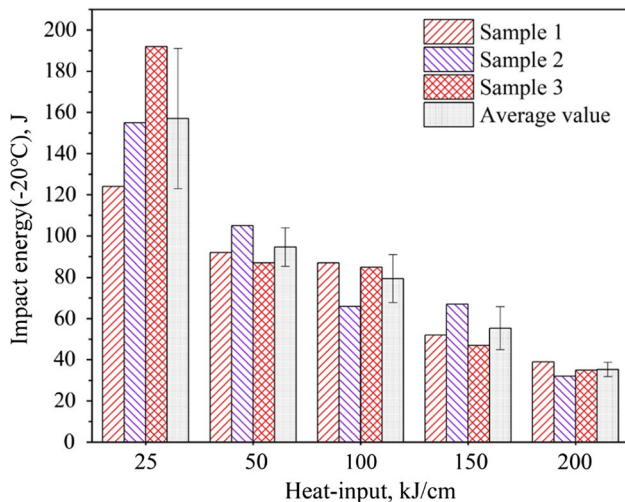
Fig. 6 Impact energy under different heat input conditions

significantly. When the heat input reach 200 kJ/cm, the value is only ~40 J. Although the high heat input is not helpful for the impact energy, the investigated steel still maintains a favorable low-temperature impact energy within 150 kJ/cm, because according to the Chinese national standard GB/T712-2011, a favorable impact toughness value of CGHAZ at any heat inputs should be greater than 46 J at −20℃. Figure 7 shows the typical loading force-time curves under different heat inputs based on the instrumented impact test. The peak loading force can reflect the total impact performance, and has a negative correlation with the heat input. As can be seen from Fig. 7, when the heat input is lower, the loading force drops gently, and when the heat input is higher, the loading force dropps rapidly and even presents a cliff-like trend. This is basically consistent with the negative effect of high heat input on the total impact energy. It is generally believed that the total impact energy is composed of the crack initiation energy and propagation energy, and when the loading force reaches the peak value, the crack initiation starts to proceed [24, 28]. Figure 7f indicates that as the heat input increases, the proportion of the crack initiation energy increases, while the propagation energy presents an opposite trend. It can be seen that the essence of heat input on impact performance depends on its effect on crack initiation energy and propagation energy. Therefore, it is necessary to analyze the influencing factors and mechanism of crack initiation and propagation.

3.3 Crack Initiation

Figure 8 shows the electronic scanning morphologies of the impact fracture of the typical samples under different heat inputs. It can be seen that a large number of dimples are observed with massive tearing ridges in the impact fracture

under the heat inputs of 25–100 kJ/cm as shown in the yellow dashed boxes and the red arrows in the images. The microstructure is undoubtedly conducive to the improvement of impact toughness. However, when the heat inputs increase to 150-200 kJ/cm, the fracture morphologies are dominated by obvious cleavage fracture planes as shown by the blue arrows in the figures. The increase of cleavage planes indicates the deterioration of impact toughness under high heat input conditions. In addition, most of the observed cleavage planes spreads around in a river pattern at some specific central points as shown by the white arrows in the figures. Related references pointed out that this is the typical fracture morphology related to the carbides or M–A constituents during crack initiation process [9, 23]. Based on 10 images at 200x field of view in the fiber area of each fracture surface, the ductile appearance ratio at different heat inputs was processed by Image-Pro Plus 6.0 software. The results are shown in Fig. 8(f). As can be seen from Fig. 8(f), the ductile appearance ratio in fiber areas of the fracture surface decreases gradually with the increase of heat input, which is consistent with the decreasing ratio of propagation energy in Fig. 7, suggesting a disadvantage for impact toughness.

Relative researchers believed that there are three possible compositions for M–A constituents in low carbon steel: one is a complete martensite constituent with twins and/or high dislocation density, and the second is a fully retained austenite phase with stacking defects. The third is a mixed constituent of austenite and martensite phases [10, 34, 35]. The M–A constituents observed based on TEM technology under the condition of 100 kJ/cm heat input are shown in Fig. 9. It can be seen that the M–A constituents under the experimental conditions presents both twin martensite constituents (as shown in Fig. 9a,b) and complete body-centered cubic martensite structure (as shown in Fig. 9c, d). This is basically in line with the researches of Lan and Lambert et al. [10, 35].

The influence of carbon atoms on the formation of M–A constituents is critical. The morphology of M–A constituents and the change of carbon contents based on EPMA technology are shown in Fig. 10a. To be precise, the M–A constituents involved in Fig. 10 are mainly the carbide enrichment that may contain M–A constituents because the carbides and M–A islands are often mixed together. Generally, it is difficult to distinguish accurately under both optical and electronic microscopes. However, as a brittle phase, the carbides and M–A islands have the similar critical effect on crack initiation. This is why the twin martensite and complete martensite are also defined as M–A islands in related studies [10, 34, 35]. As can be seen from Fig. 10a, the enrichment of carbon atoms is obvious. In fact, the carbon atoms can be enriched in the retained austenite, improving the stability of the retained austenite, reducing the starting temperature of martensite in the local regions, which creates
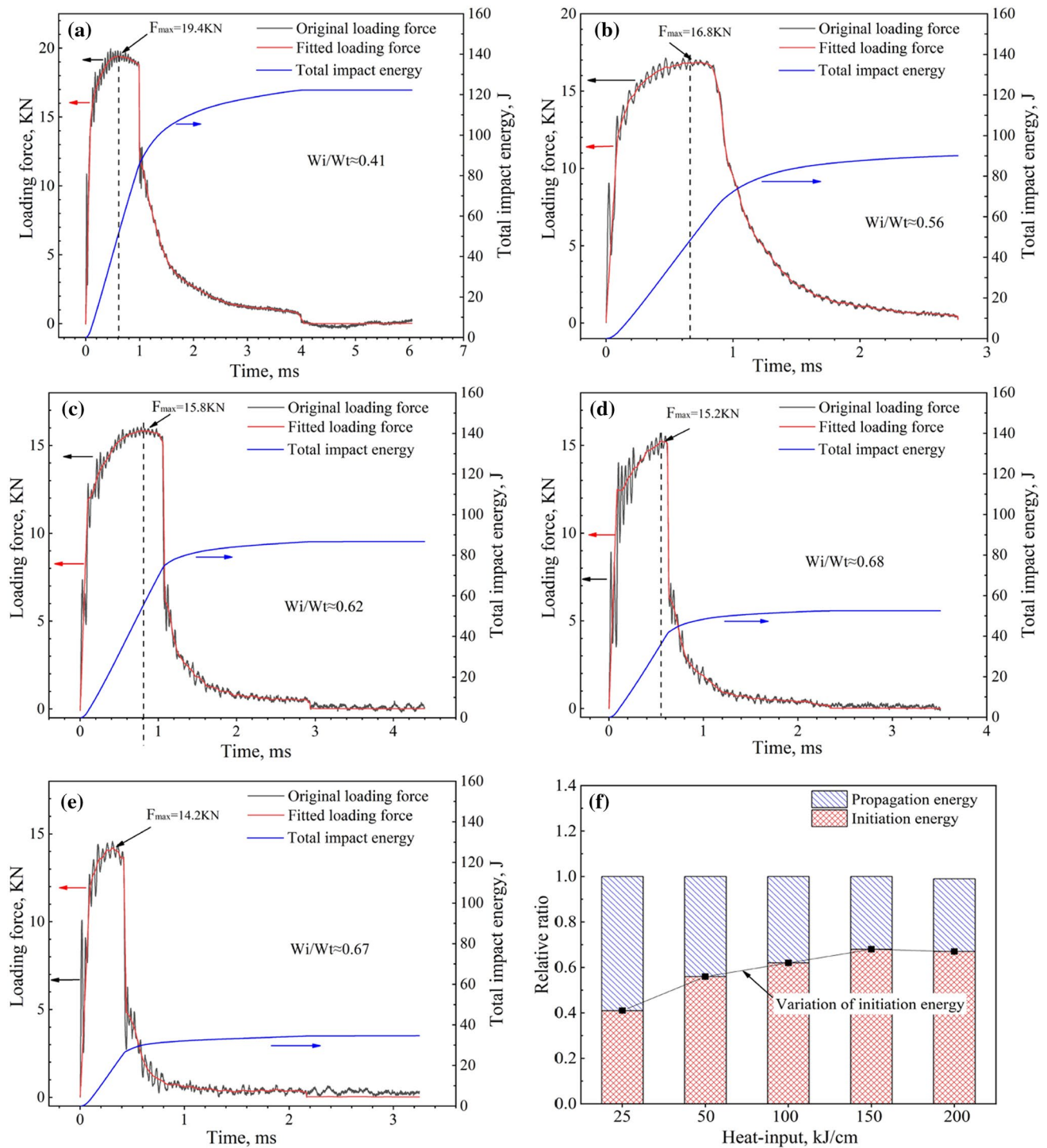
Fig. 7 Variation of loading force and total impact energy with time in the typical samples **a–e**. The ratio of initiation and propagation energy to total absorbed energy in **a–e** under different heat input conditions is shown in **f**. **a** 25 kJ/cm; **b** 50 kJ/cm; **c** 100 kJ/cm; **d** 150 kJ/cm; **e** 200 kJ/cm. Wi/Wt refers to the ratio of initiation energy to total impact absorbed energy

a possible condition for the twin M–A constituents [10]. Figure 10b shows the typical morphologies and volume fractions of the carbide enrichment that may contain M–A constituents under different heat inputs. It can be seen that as the heat input increases, the volume fraction of the carbide enrichment decreases gradually. However, the morphology changes from strip to blocky shape, and the trend of adhesion increases. The heat input is the main factor affecting
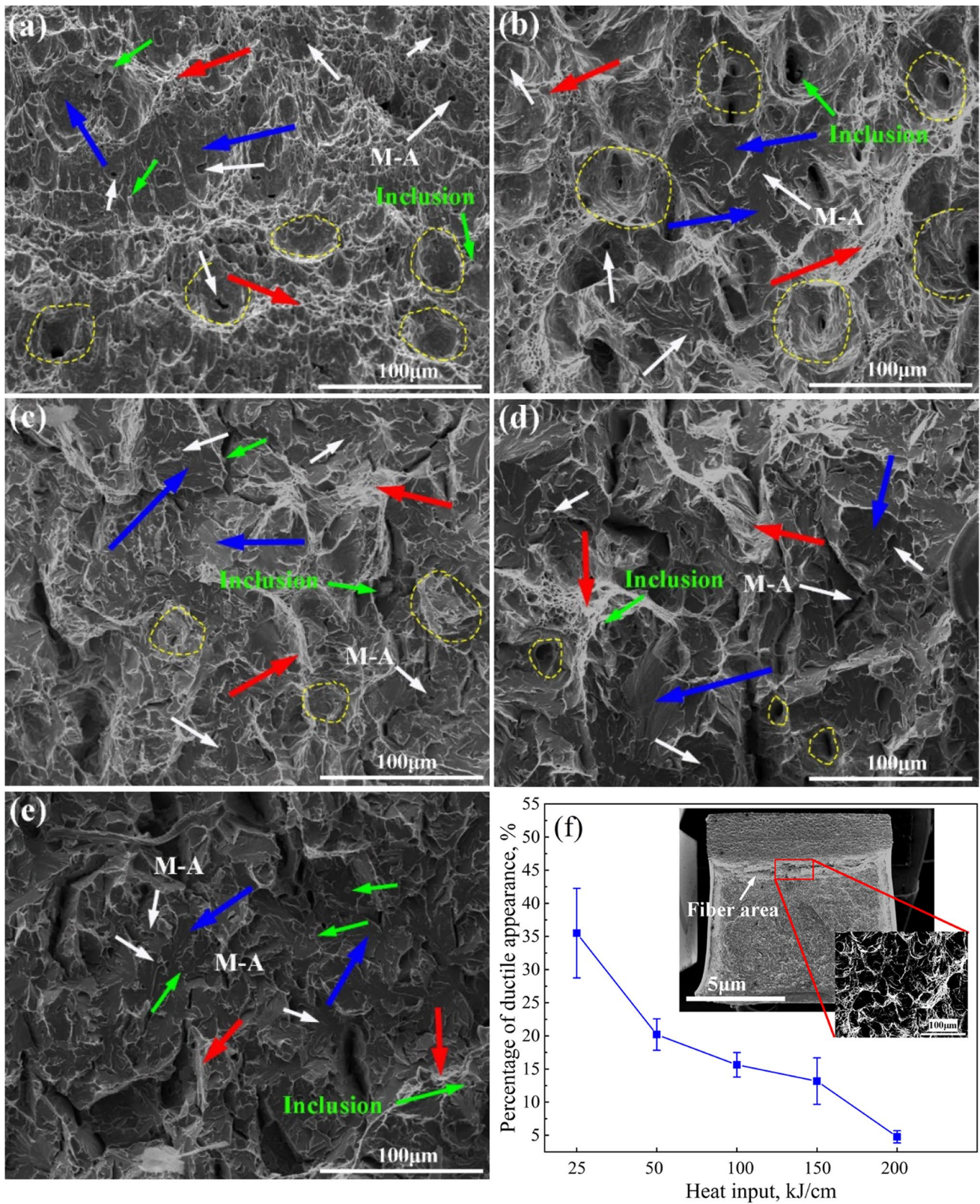
Fig. 8 Impact fracture morphologies of typical specimens under different heat inputs. **a** 25 kJ/cm; **b** 50 kJ/cm; **c** 100 kJ/cm; **d** 150 kJ/cm; **e** 200 kJ/cm; **f** Ductile appearance ratio in fiber area of the fracture surface with different heat inputs
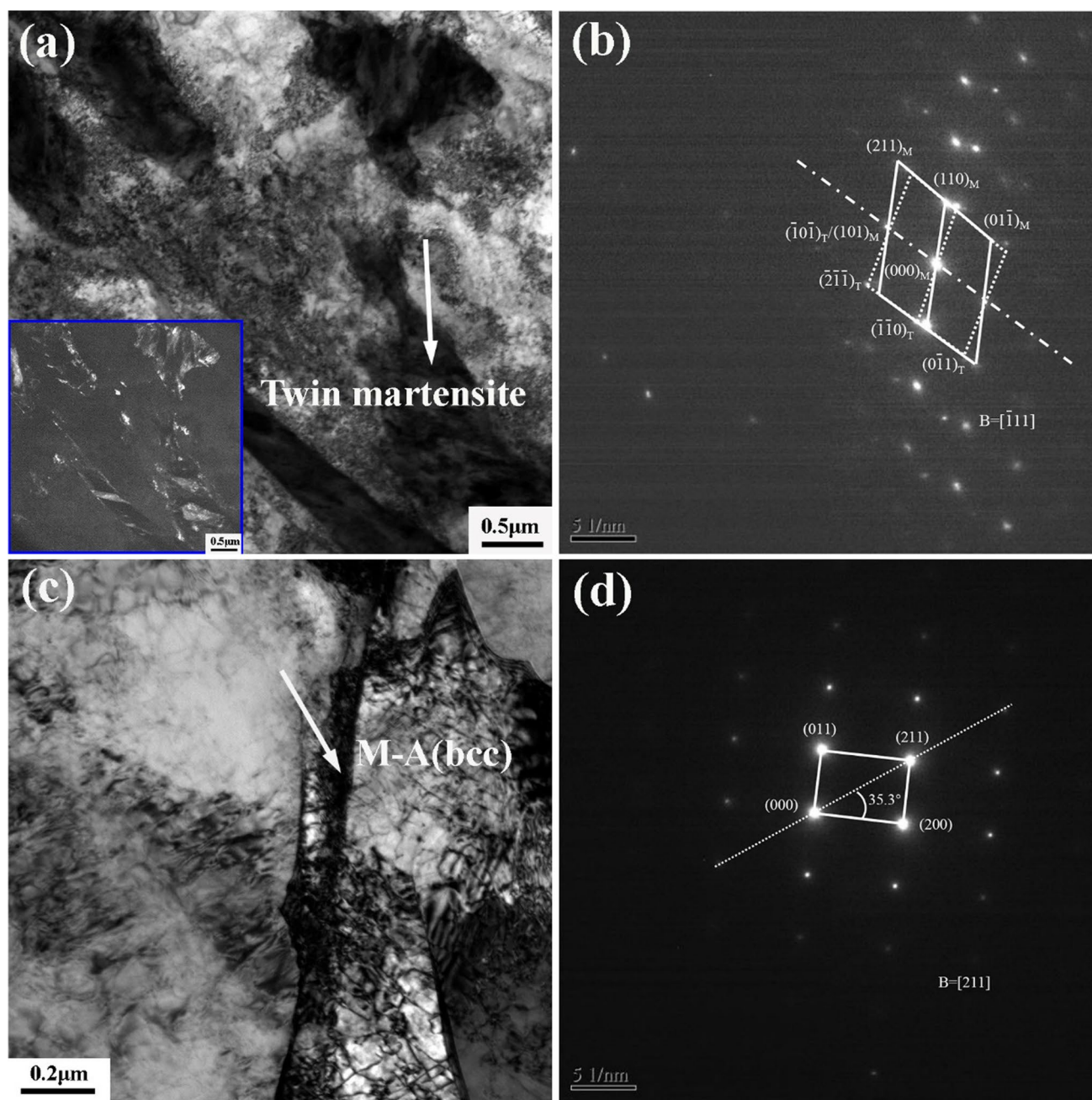
Fig. 9 Typical morphologies **a, c** and SAD patterns **b, d** of M–A constituents based on 100 kJ/cm heat input. The white arrows in figures **a, c** are the positions corresponding to the SAD patterns in figures **b,** **d**; the embedded image in **a** is the corresponding dark field morphology of twin martensite

the morphology and size of the carbide enrichment when the chemical composition of the BM is fixed beacuse the carbide enrichment tends to precipitate at grain boundaries [24]. The higher heat inputs will cause the morphology to change with the coarse microstructure and the coarse prior austenite grains also make it easy for carbon atoms to segregate at the grain boundaries. Li et al. also believed that the coarser the prior austenite grains, the coarser are the

M–A constituents [25]. In addition, under high heat input conditions, the carbon atoms tend to be enriched at grain boundaries due to increased diffusion efficiency. In other words, high heat input conditions allow enough time for carbons to diffuse from the center of the grain to the grain boundary to form coarse carbon domains. Therefore, with the increase of heat input, the size of M–A constituents or carbides increases. The investigated results are consistent
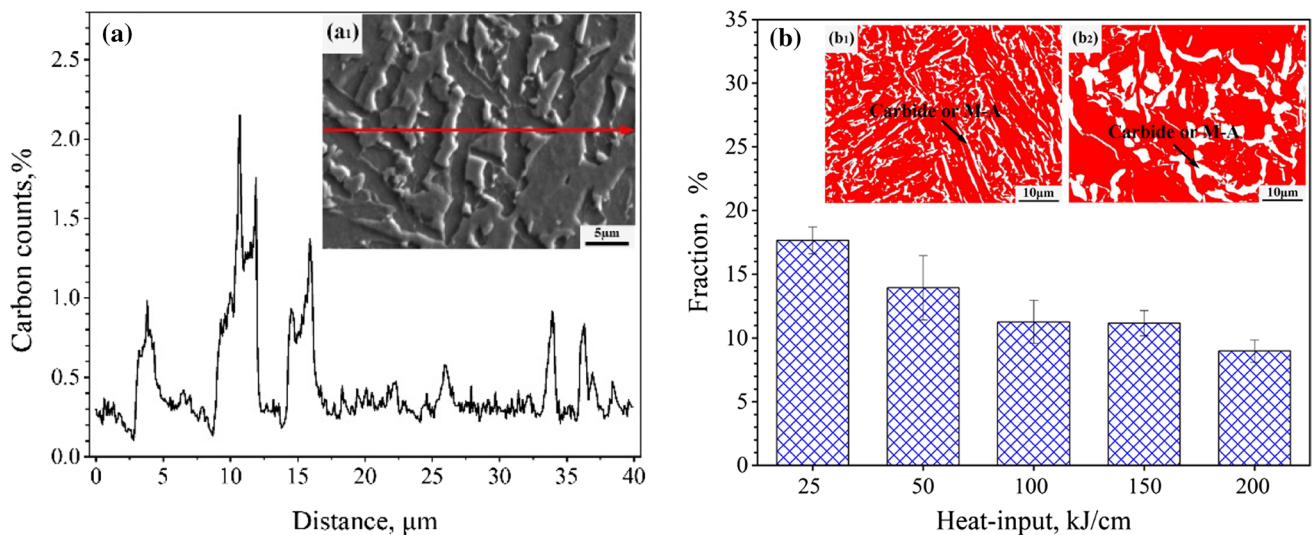
Fig. 10 Carbon contents in carbide enrichment **a** based on heat input of 100 kJ/cm and the volume fraction of carbides under different heat input conditions **b**. The embedded figures indicate the line scanning path (a_1) and morphology obtained by image software at different heat inputs. (b_1) 25 kJ/cm and (b_2) 200 kJ/cm

with the studies of Xie and Chandran Ramachandran et al. [16, 22].

Although the crack initiation energy increases with the decrease of the volume fraction of carbides at high heat input, the coarse blocky carbides or M–A constituents actually increase the risk of crack initiation. Kim et al. pointed out that both the increase in the volume fraction and the coarse morphologies of the M–A constituents have an critical effect on the low-temperature impact toughness [17]. Under high heat input conditions, the reason for the increase of crack initiation absorbed energy is likely to originate from the tearing and stripping process between multiple M–A constituents [23]. Relevant researchers proposed four mechanisms for the influence of M–A constituents on crack initiation [13, 28, 36, 37]: (1) As the hardened phase, M–A constituent itself has a tendency of stress concentration, causing the crack initiation to form in itself and then propagate to the matrix; (2) Because the M–A constituent has a higher hardness than the matrix, it is easy to cause stress concentration at the interface with the adjacent matrix, causing crack initiation at the edge of M–A constituent; (3) The high-carbon martensite in M–A constituent originates from the transformation of retained austenite at low temperature. The residual stress caused by the phase transformation leads to the stress concentration in the surrounding matrix, causing cracks to initiate; (4) The debonding of the non-coherent interface between M–A constituent and the matrix leads to the initiation of microcracks. It can be seen that the morphology of the M–A constituent has an adverse effect on the crack initiation. At high heat input conditions, the coarse carbides or M–A constituents as well as GBF may be the main factors causing the decrease of toughness [25].

In addition, it is worth noting that under different heat input (25–200 kJ/cm) conditions, some micro-inclusions appear to promote crack initiation as shown in Fig. 8. In fact, inclusions can be used as the source of crack initiation to affect the impact toughness, acting as the similar role of coarse M–A constituents or carbides [9]. The difference is that although some inclusions can be used as the source of crack initiation to reduce the absorbed energy, some certain effective inclusions can also induce AF or multi-directional bainite nucleation, which is conducive to the accumulation of crack absorbed energy [5, 7, 19]. In this study, the samples still present favorable low-temperature impact toughness at high heat input, which is directly related to the large amount of AF and multi-directional bainite microstructure. It can be seen that the effective control of inclusions during the melting process is the key factor for CGHAZ to obtain more AF or multi-directional bainite after welding thermal cycle. Therefore, it is very important to analyze the morphology, composition and size of the effective inclusions in the matrix. Figures 11 and 12 show the typical morphology, size and composition of inclusions based on EPMA technology. As can be seen, the typical inclusions that can induce the formation of acicular microstructure are generally round, with the size of ~2 μm, and the compositions are mainly Al-Ti-Mn-O. It is worth noting that the content of Ti in most of the inclusions always accounts for a larger proportion as shown in Figs. $11b_3$, e_3 and 12a, b. This is consistent with the research on AF nucleation by Ti-containing complex oxide inclusions mentioned in most studies [7, 38–40]. The influence of inclusions on impact toughness is twofold. Although the crack initiation can be stimulated by inclusions, the carbides or M–A constituents appear to have a greater impact
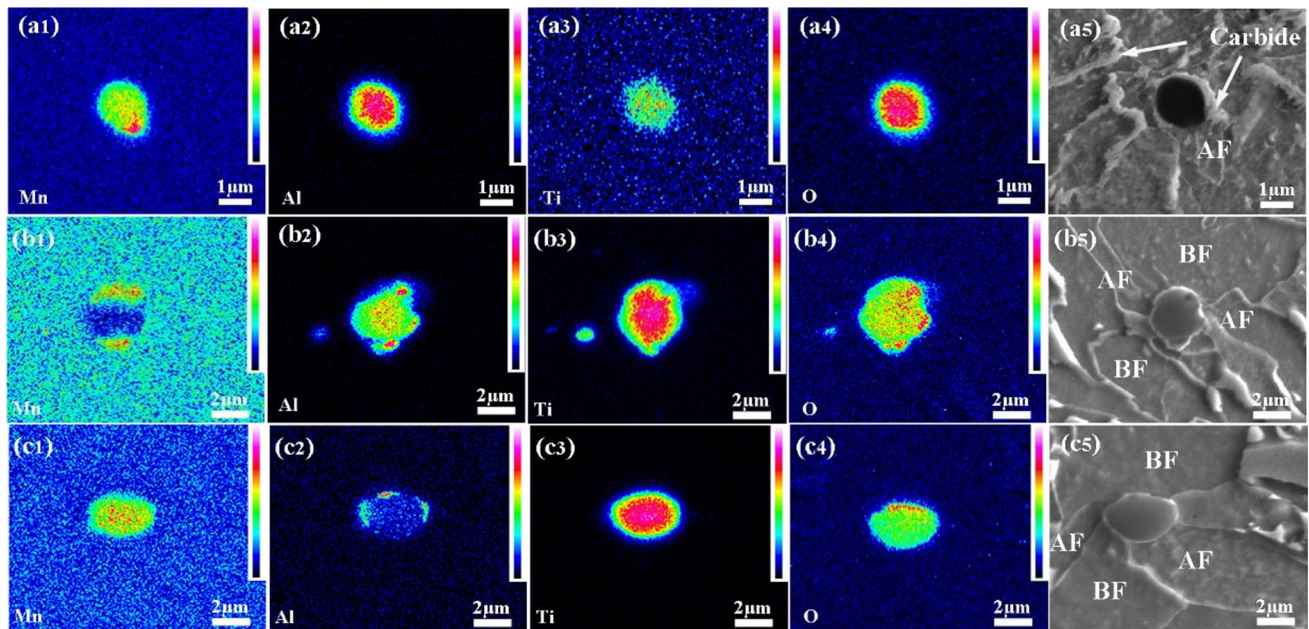
Fig. 11 Morphology and composition of typical inclusions with AF potential under different heat inputs. a_1-a_5 25 kJ/cm; b_1-b_5 50 kJ/cm; c_1-c_5 100 kJ/cm
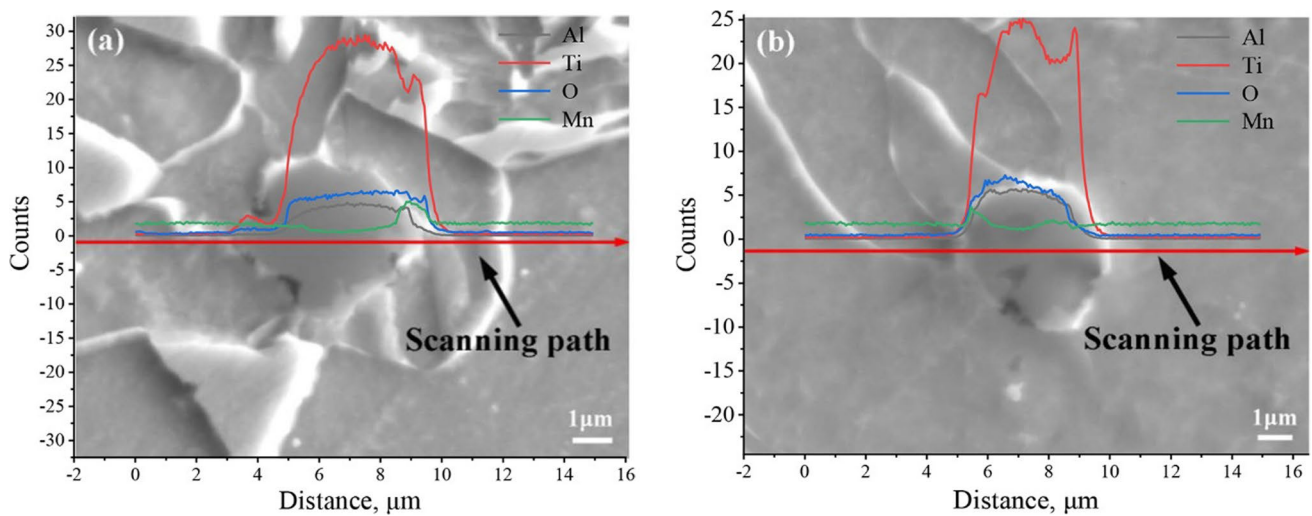

Fig. 12 Line scanning results of typical inclusions with AF potential in CGHAZ at heat inputs of 150 kJ/cm **a** and 200 kJ/cm **b** based on EPMA technology

as shown in above analysis. Therefore, reasonable control of the characteristics of inclusions to induce more acicular microstructure is conducive to the improvement of impact toughness during high heat input welding process.

3.4 Crack Propagation

Figure 13 shows the distribution of high-angle grain boundaries in the micro regions under different heat inputs based on

the EBSD technology. The red solid lines represent the misorientation greater than 15°, which is generally considered as the high-angle grain boundaries [4, 28, 36]. As can be seen from Figs. 13a-c, the GB/AF microstructures were dominated by high-angle grain boundaries and the misorientation inside the boundary ferrite is obviously lower. According to the scanning position of the blue solid lines in Fig. 13c, the statistical data of the misorientation in Fig. 13d shows that the misorientation in GBF microstructure is generally within
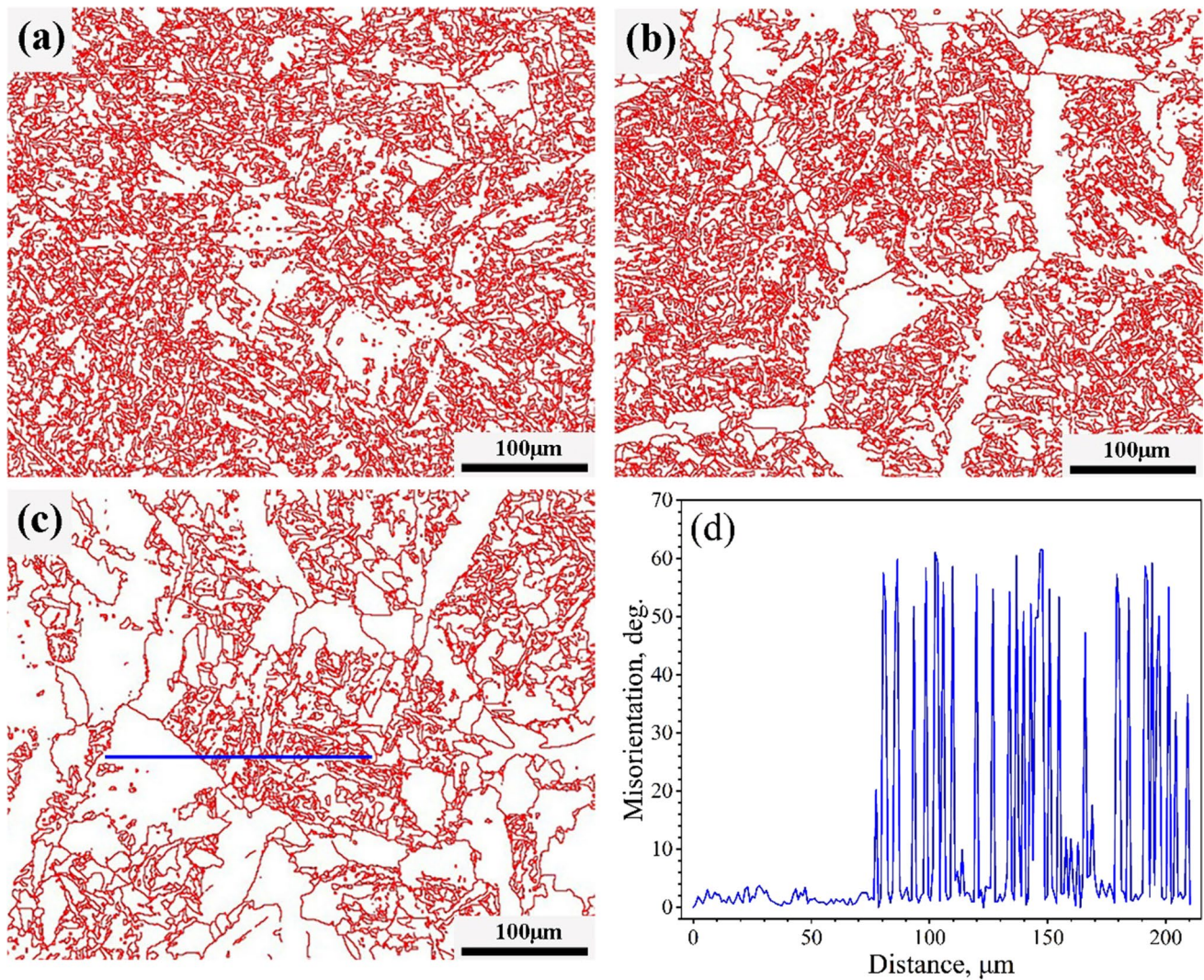
Fig. 13 Distribution of grian boundary of CGHAZ at different heat inputs based on EBSD technology. **a** 25 kJ/cm, **b** 100 kJ/cm and **c** 200 kJ/cm. The solid red lines in the figures refer to the boundary misorientation greater than 15°. The solid blue line in **c** is the scanning position of **d**

5°, while the misorientation of acicular microstructure in the prior austenite grains is generally 50–60°. This is consistent with the analysis of Ramachandran et al. [22]. As the heat input increases, the distribution probability of the misorientation less than 5° is increased, while the misorientation greater than 50° presents a decreasing trend as shown in Fig. 14. The large amount of GBF precipitation caused by the increase of heat input is the main reason for the increase of low-angle grain boundaris, which may greatly affect the impact performance of CGHAZ.

Figure 15 shows the morphologies of the crack propagation paths. It can be seen that the cracks consisted of initial cracks (as shown by the blue arrows in Fig. 15) and secondary cracks (as shown by the red arrows in Fig. 5) at both lower and higher heat inputs, and the propagation paths are dominated by transgranular fracture model. In addition, it is

worth noting that the AF (200 kJ/cm) is more conducive to causing the crack propagation to be deflected or arrested than GB (25 kJ/cm), while massive blocky GBF microstructure can cause the crack paths to almost propagate along straight direction by the transgranular fracture mode at high heat input (200 kJ/cm). According to the experimental results shown in Fig. 13, the interior of GBF is mainly dominated by low-angle grain boundaries within 5°. The deflection and arrest of crack propagation are to a large extent determined by the high-angle grain boundary misorientation, while the low-angle boundary has a weaker effect on the crack propagation path [28, 41]. Generally, the grain boundary misorientation greater than 15° can be defined as effective grains in an unit area, and the effective grain size is a very important parameter to characterize the crack arrest ability [28]. Therefore, the high density of low-angle grain boundaries in GBF
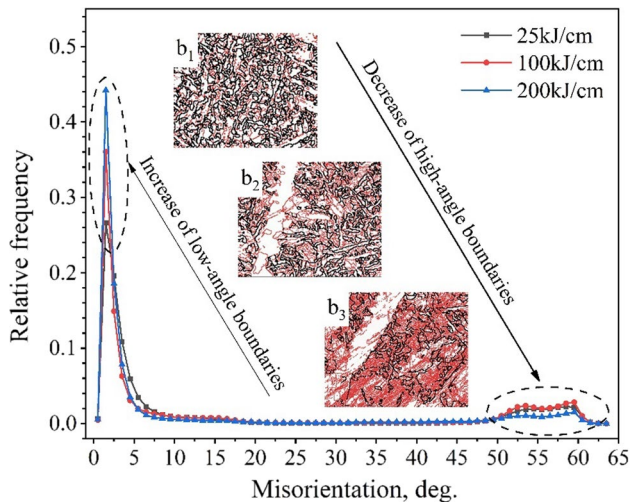
Fig. 14 Distribution of grain boundary misorientation with different heat inputs. b_1 25 kJ/cm, b_2 100 kJ/cm, b_3 200 kJ/cm. The red and black lines in the embedded figures represent misorientation less than 5° and greater than 50° respectively

microstructure is not beneficial to improve the toughness, which explain why the GBF always causes secondary cracks as shown in the Fig. 15.

4 Conclusions

In this paper, a low-carbon high-strength plate with the yield strength of ~690 MPa was obtained in the laboratory based on "oxide metallurgy" and TMCP technology. The microstructure and low-temperature impact toughness of CGHAZ at different heat inputs were characterized by TEM, EBSD, EPMA and other methods. The conclusions are as follows:

1. Under lower heat input of 25 kJ/cm, the average value of impact energy in simulated CGHAZ at −20 °C was ~158 J. With the increase of the heat input, the average values decreased. However, even at the heat input of 150 kJ/cm, the CGHAZ still presented a favorable low-temperature impact toughness of ~60 J.

2. The coarse carbides or M–A constituents provided convenient conditions for the initiation of cracks. At high heat input conditions, the typical M–A constituents detected by TEM could be body-centered cubic martensite structure or twinned martensite structure. With the increase of heat input, the sensitivity of crack initiation increased obviously because the morphology of coarse carbides or M–A constituents changed from strip to bulk gradually.

3. The Ti-containing inclusions could be used as the source of cracks to stimulate crack initiation, while they could also induce the formation of AF to hinder the crack propagation effectively, which improved the crack propagation absorbed energy. Therefore, reasonable control of the characteristics of inclusions to induce more AF was conducive to the improvement of impact toughness during high heat input welding process.

4. As the heat input increased, the coarse GBF with more low-angle grain boundaries increased obviously, which was not conducive to the crack propagation absorbed energy. The massive blocky GBF was mainly responsible for the deterioration of impact toughness in CGHAZ under high heat input conditions.

5. The effective activation energies of GBF and AF/GB were obtained by the dilatometric test at different heat inputs, which were ~175 kJ/mol and ~227 kJ/mol. This explained the reason for the preferential precipitation of GBF under high heat input conditions from the perspective of kinetics.

Fig. 15 Propagation paths of microcracks at heat inputs of 25 kJ/cm **a** and 200 kJ/cm **b**. The embedded images show the corresponding morphologies under electron microscope
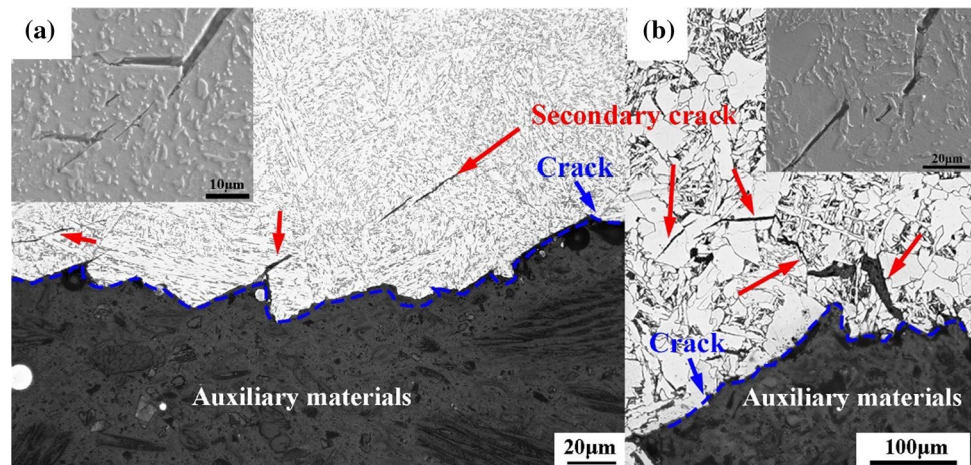
Author Contributions YY: Conceptualization, Methodology, Formal analysis, Writing-original draft, Writing-review & editing, Data curation. XJ, YM: Investigation, Validation, Methodology, Formal analysis. PW: Methodology, Validation, Resources, Supervision. FZ: Methodology, Funding acquisition, Supervision, Resources.

Data Availability The raw/processed data required to reproduce these findings cannot be shared at this time as the data also forms part of an ongoing study.

Declarations

Conflict of interest The authors declare that they have no known competing financial interests or personal relationships that could have appeared to influence the work reported in this paper.

References

1. L. Lan, X. Kong, Z. Chang, C. Qiu, D. Zhao, Microstructure, composition, and impact toughness across the fusion line of high-strength bainitic steel weldments. Metall. Mater. Trans. A **48**, 4140–4153 (2017)

2. P. Haslberger, S. Holly, W. Ernst, R. Schnitzer, Microstructure and mechanical properties of high-strength steel welding consumables with a minimum yield strength of 1100 MPa. J. Mater. Sci. **53**, 6968–6979 (2018)

3. S.Y. Shin, K. Oh, K.B. Kang, S. Lee, Effects of complex oxides on charpy impact properties of heat affected zones of two API X70 linepipe steels. ISIJ Int. **49**, 1191–1199 (2009)

4. X. Xi, J. Wang, L. Chen, Z. Wang, On the role of Cu addition in toughness improvement of coarse grained heat affected zone in a low carbon high strength steel. J. Mater. Sci. **55**, 10863–10877 (2020)

5. Z.-H. Song, H.-Y. Song, H.-T. Liu, Effect of cooling route on microstructure and mechanical properties of twin-roll casting low carbon steels with an application of oxide metallurgy technology. Mater. Sci. Eng. A **800**, 2–12 (2021)

6. K. Zhu, Z. Yang, Effect of magnesium on the austenite grain growth of the heat-affected zone in low-carbon high-strength steels. Metall. Mater. Trans. A **42**, 2207–2213 (2011)

7. X. Wang, C. Wang, J. Kang, G. Yuan, R.D.K. Misra, G. Wang, Improved toughness of double-pass welding heat affected zone by fine Ti-Ca oxide inclusions for high-strength low-alloy steel. Mater. Sci. Eng. A **780**, 2–11 (2020)

8. L. Lan, C. Qiu, D. Zhao, X. Gao, L. Du, Analysis of microstructural variation and mechanical behaviors in submerged arc welded joint of high strength low carbon bainitic steel. Mater. Sci. Eng. A **558**, 592–601 (2012)

9. R. Cao, J. Li, D.S. Liu, J.Y. Ma, J.H. Chen, Micromechanism of decrease of impact toughness in coarse-grain heat-affected zone of HSLA steel with increasing welding heat input. Metall. Mater. Trans. A **46**, 2999–3014 (2015)

10. L. Lan, C. Qiu, D. Zhao, X. Gao, L. Du, Analysis of martensite–austenite constituent and its effect on toughness in submerged arc welded joint of low carbon bainitic steel. J. Mater. Sci. **47**, 4732–4742 (2012)

11. K. Poorhaydari, B.M. Patchett, D.G. Ivey, Transformation twins in the weld HAZ of a low-carbon high-strength microalloyed steel. Mater. Sci. Eng. A **435–436**, 371–382 (2006)

12. J. Hu, L.-X. Du, J.-J. Wang, C.-R. Gao, Effect of welding heat input on microstructures and toughness in simulated CGHAZ of V-N high strength steel. Mater. Sci. Eng. A **577**, 161–168 (2013)

13. J. Hu, L.-X. Du, H. Xie, F.-T. Dong, R.D.K. Misra, Effect of weld peak temperature on the microstructure, hardness, and transformation kinetics of simulated heat affected zone of hot rolled ultra-low carbon high strength Ti-Mo ferritic steel. Mater. Des. **60**, 302–309 (2014)

14. Q. Jiang, Y. Li, J. Wang, L. Zhang, Microstructural characteristics and prediction of austenite grain size in heat affected zone of high strength low alloy steel. ISIJ Int. **51**, 269–273 (2011)

15. L. Lan, C. Qiu, D. Zhao, X. Gao, L. Du, Effect of reheat temperature on continuous cooling bainite transformation behavior in low carbon microalloyed steel. J. Mater. Sci. **48**, 4356–4364 (2013)

16. H. Xie, L.X. Du, J. Hu, G.S. Sun, H.Y. Wu, R.D.K. Misra, Effect of thermo-mechanical cycling on the microstructure and toughness in the weld CGHAZ of a novel high strength low carbon steel. Mater. Sci. Eng. A **639**, 482–488 (2015)

17. I. Kim, H. Nam, M. Lee, D. Nam, Y. Park, N. Kang, Effect of martensite-austenite constituent on low-temperature toughness in YS 500 MPa grade steel welds. Metals **8**, 2–11 (2018)

18. M. Amraei, A. Ahola, S. Afkhami, T. Björk, A. Heidarpour, X.-L. Zhao, Effects of heat input on the mechanical properties of butt-welded high and ultra-high strength steels. Eng. Struct. **198**, 2–15 (2019)

19. L.-Y. Xu, J. Yang, R.-Z. Wang, Y.-N. Wang, W.-L. Wang, Effect of Mg content on the microstructure and toughness of heat-affected zone of steel plate after high heat input welding. Metall. Mater. Trans. A **47**, 3354–3364 (2016)

20. Y. Liu, G. Li, X. Wan, H. Wang, K. Wu, R.D.K. Misra, The role of Cu and Al addition on the microstructure and fracture characteristics in the simulated coarse-grained heat-affected zone of high-strength low-alloy steels with superior toughness. Mater. Sci. Technol. **33**, 1750–1764 (2017)

21. C. Li, Y. Wang, T. Han, B. Han, L. Li, Microstructure and toughness of coarse grain heat-affected zone of domestic X70 pipeline steel during in-service welding. J. Mater. Sci. **46**, 727–733 (2010)

22. D. Chandran Ramachandran, J. Moon, C.-H. Lee, S.-D. Kim, J.-H. Chung, E. Biro, Y.-D. Park, Role of bainitic microstructures with M–A constituent on the toughness of an HSLA steel for seismic resistant structural applications. Mater. Sci. Eng. A **801**, 2–11 (2021)

23. P. Mohseni, J.K. Solberg, M. Karlsen, O.M. Akselsen, E. Østby, Investigation of mechanism of cleavage fracture initiation in intercritically coarse grained heat affected zone of HSLA steel. Mater. Sci. Technol. **28**, 1261–1268 (2014)

24. Y. Zhou, T. Jia, X. Zhang, Z. Liu, R.D.K. Misra, J. Mater. Process. Technol. **219**, 314–320 (2015)

25. X. Li, X. Ma, S.V. Subramanian, C. Shang, R.D.K. Misra, Influence of prior austenite grain size on martensite-austenite constituent and toughness in the heat affected zone of 700 MPa high strength linepipe steel. Mater. Sci. Eng. A **616**, 141–147 (2014)

26. L. Zhang, Y. Li, J. Wang, Q. Jiang, Effect of acicular ferrite on cracking sensibility in the weld metal of Q690 + Q550 high strength steels. ISIJ Int. **51**, 1132–1136 (2011)

27. M. Shi, P. Zhang, F. Zhu, Toughness and microstructure of coarse grain heat affected zone with high heat input welding in Zr-bearing low carbon steel. ISIJ Int. **54**, 188–192 (2014)

28. L. Lan, C. Qiu, D. Zhao, X. Gao, L. Du, Microstructural characteristics and toughness of the simulated coarse grained heat affected zone of high strength low carbon bainitic steel. Mater. Sci. Eng. A **529**, 192–200 (2011)

29. C. Gupta, G.K. Dey, J.K. Chakravartty, D. Srivastav, S. Banerjee, A study of bainite transformation in a new CrMoV steel under continuous cooling conditions. Scripta Mater. **53**, 559–564 (2005)

30. E.J. Mittemeijer, Analysis of the kinetics of phase transformations. J. Mater. Sci. Technol. **27**, 3977–3987 (1992)

31. C. Liu, X. Di, C. Chen, X. Guo, Z. Xue, A bainite transformation kinetics model and its application to X70 pipeline steel. J. Mater. Sci. **50**, 5079–5090 (2015)

32. S.-J. Lee, J.-S. Park, Y.-K. Lee, Effect of austenite grain size on the transformation kinetics of upper and lower bainite in a low-alloy steel. Scripta Mater. **59**, 87–90 (2008)

33. F. Liu, S.J. Song, F. Sommer, E.J. Mittemeijer, Corrigendum to "Evaluation of the maximum transformation rate for analyzing solid-state phase transformation kinetics". Acta Mater. **58**, 6176–6190 (2010)

34. E. Bonnevie, G. Ferrière, A. Ikhlef, D. Kaplan, J.M. Orain, Morphological aspects of martensite–austenite constituents in inter-critical and coarse grain heat affected zones of structural steels. Mater. Sci. Eng. A **385**, 352–358 (2004)

35. A. Lambert, J. Drillet, A.F. Gourgues, T. Sturel, A. Pineau, Microstructure of martensite–austenite constituents in heat affected zones of high strength low alloy steel welds in relation to toughness properties. Sci. Technol. Weld. Join. **5**, 168–173 (2013)

36. A. Lambert-Perlade, A.F. Gourgues, J. Besson, T. Sturel, A. Pineau, Mechanisms and modeling of cleavage fracture in simulated heat-affected zone microstructures of a high-strength low alloy steel. Metall. Mater. Trans. A **35**, 1039–1053 (2004)

37. Y. Li, T.N. Baker, Effect of morphology of martensite–austenite phase on fracture of weld heat affected zone in vanadium and niobium microalloyed steels. Mater. Sci. Technol. **26**, 1029–1040 (2013)

38. J.M. Gregg, H.K.D.H. Bhadeshia, Titanium-rich mineral phases and the nucleation of bainite. Metall. Mater. Trans. A **25**, 1603–1611 (1994)

39. J.-H. Shim, Y.W. Cho, S.H. Chung, J.D. Shim, D.N. Lee, Nucleation of intragranular ferrite at Ti2O3 particle in low carbon steel. Acta Mater. **47**, 2751–2760 (1999)

40. Y. Kang, S. Jeong, J.-H. Kang, C. Lee, Factors affecting the inclusion potency for acicular ferrite nucleation in high-strength steel welds. Metall. Mater. Trans. A **47**, 2842–2854 (2016)

41. A. Lambert-Perlade, A.F. Gourgues, A. Pineau, Austenite to bainite phase transformation in the heat-affected zone of a high strength low alloy steel. Acta Mater. **52**, 2337–2348 (2004)